

Pitch-Angle Feedback Control of a Biologically Inspired Flapping-Wing Microrobot

Néstor O. Pérez-Arancibia, Pakpong Chirarattananon, Benjamin M. Finio, and Robert J. Wood

Abstract—This paper presents the first experimental results on pitch-angle control of a flapping-wing microrobot. First, we describe a control method by which torques can be modulated to change the pitch orientation of the microrobot. The suitability of the proposed method is demonstrated through hardware-in-the-loop experiments, employing a static experimental setup capable of measuring instantaneous torques produced by enforced flapping patterns. Then, using the information learned from the static hardware-in-the-loop experiments, controlled pitch rotation experiments are performed. The pitch-angle is measured using a motion capture system. Compelling results are presented to validate the chosen approach.

I. INTRODUCTION

Control methods for modulating forces generated by flapping-wing microrobots have been described in [1] and [2], and control strategies for enforcing trajectories in one degree of freedom (altitude) have been presented in [3]. The flying microrobot used in those works was developed and fabricated based upon designs which previously demonstrated the ability to liftoff [4]. This robot is under-actuated and complete autonomy is not feasible without the addition of steering actuators to the robot's thoracic mechanism [5]. Nonetheless, in this article, we empirically demonstrate that the original design can be actuated so that the pitch-angle can be controlled.

As described in [4], the main components of the microrobot are the airframe, the bimorph piezoelectric driving actuator, used to transduce electrical into mechanical power, and the mechanical transmission that maps the actuator output displacement to the flapping angle of the wings. The robot's wings are connected to the transmission through flexible hinges that allow the wings to rotate. This rotation is referred to as passive rotation, because this is not produced by the action of actuators, but by the inertial and aerodynamic forces generated by the flapping of the wings [6]. When driven with periodic flapping, the microrobot produces instantaneous flight forces that can be modulated by varying the amplitude and/or frequency of the flapping angle (also referred to as the stroke angle) [1], [2], [3].

The results on pitch angle control presented here represent a key step towards the final goal of stable flight. This is accomplished in two stages. Similar to the cases in [1], [2] and

[3], in the first stage we perform static flapping experiments from which relevant information can be gathered, using system identification methods so that controller strategies for a series of one-degree-of-freedom experiments can be devised. In the setup used in the static experiments, the most relevant component is a custom made torque sensor, which is designed using basic principles of solid mechanics [7]. This sensor enables static hardware-in-the-loop experiments, in which the ideas and methods proposed for pitch-angle control can be properly evaluated. In the second stage, a microrobotic fly is constrained so that it is allowed to vary the value of the pitch-angle only, i.e., the resulting system has one rotational degree of freedom (pitch). The required actuation for varying the pitch-angle is generated by using asymmetrical flapping patterns. Asymmetrical flapping trajectories can be produced by biasing the actuator motion dorsoventrally.

The rest of the paper is organized as follows. Section II explains the microrobotic flapping mechanism and the experimental setup. Section III describes the empirical identification of the system dynamics, discusses the control strategies considered, the controller design method, and presents static hardware-in-the-loop experiments. Section IV presents experimental evidence on the suitability of the proposed schemes for pitch control, using a motion capture system. Finally, conclusions are given in Section V.

Notation:

- \mathbb{R} and \mathbb{Z}^+ denote the sets of real and non-negative integer numbers, respectively.
- The variable t is used to index discrete time, i.e., $t = \{kT_s\}_{k=0}^{\infty}$, with $k \in \mathbb{Z}^+$ and $T_s \in \mathbb{R}$. As usual, T_s is referred as the sampling-and-hold time. Depending on the context we might indistinctly write $x(t)$ or $x(k)$.
- The variable σ is used to index continuous time.
- z^{-1} denotes the discrete-time delay operator, i.e., for a signal x , $z^{-1}x(k) = x(k-1)$ and conversely $zx(k) = x(k+1)$. The symbol z also denotes the complex variable associated with the \mathcal{Z} -transform.
- s^{-1} denotes the integral operator and s is the complex variable associated with the Laplace transform.

II. DESCRIPTION OF THE MICROROBOT AND EXPERIMENTAL SETUP

A. Microrobot

In this subsection, we briefly describe the microrobot and explain the generation of flight forces and body torques. As can be seen in Fig. 1, the robot is composed of four main elements: the airframe, the actuator, the transmission and the wings. Flight forces are generated through a phenomenon referred to as passive rotation. Here, the wings are connected to

This work was partially supported by the National Science Foundation (award number CCF-0926148) and the Wyss Institute for Biologically Inspired Engineering. Any opinions, findings, and conclusions or recommendations expressed in this material are those of the authors and do not necessarily reflect the views of the National Science Foundation.

The authors are with the School of Engineering and Applied Sciences, Harvard University, Cambridge, MA 02138, USA, and the Wyss Institute for Biologically Inspired Engineering, Harvard University, Boston, MA 02115, USA, (nperez@seas.harvard.edu, chirarat@fas.harvard.edu, bfinio@fas.harvard.edu, rjwood@eecs.harvard.edu).

the mechanical transmission through flexible hinges, which allow the wings to rotate (angle $\theta(t)$ in Fig. 1). This rotation is caused by the inertial forces produced by the flapping $\varphi(t)$ and by the aerodynamic forces generated by the interaction of the wings with the air. As explained in [6], an angle θ different than 0° implies that the wings have a positive angle of attack, which causes the generation of lift forces. The microrobot was designed such that, for sinusoidal actuator displacements, drag forces are symmetric about the upstroke and downstroke and the mean lift force vector intersects the center of mass. Thus, ideally, no body torques are generated and the angles of rotation in three dimensions about the robot's center of mass (pitch, roll and yaw) should stay at 0° . This case is depicted in Fig. 2-(a).

From the free-body diagram in Fig. 1, it follows that the equation of motion along the vertical axis is simply

$$\gamma_L(\sigma) - mg = m\ddot{x}(\sigma), \quad (1)$$

where m is the mass of the robot, g is the gravitational acceleration constant and $\gamma_L(\sigma)$ is the instantaneous lift force generated by the flapping wings. In some cases, an additional dissipative body drag term $\kappa_d\dot{x}(\sigma)$ could be added to the right side of (1), where κ_d is a constant to be identified experimentally. Note that the system, as described by (1), is unstable because its input-output representation has two poles at 0.

As described in [1], [2] and [6], the lift force $\gamma_L(\sigma)$ is a nonlinear function of the frequency and amplitude of the flapping angle φ . Also as discussed in [1], [2] and [6], for sinusoidal inputs, instantaneous lift forces $\gamma_L(\sigma)$ typically oscillate around some non-zero mean force, crossing zero periodically. Therefore, ascent occurs when the average lift force, $\Gamma_L(\sigma)$ in Fig. 1, is larger than mg , and hovering occurs when the average lift force $\Gamma_L(\sigma)$ equals mg . When using digital computers for measurement and control, $\gamma_L(\sigma)$ is sampled at a fixed rate T_s . Thus, the sampled discrete-time version of $\gamma_L(\sigma)$, $\gamma_L(t)$, can be used to estimate $\Gamma_L(\sigma)$ as $\Gamma_L(t) = (1/N_L) \sum_{i=0}^{N_L-1} \gamma_L(t - iT_s)$, where $0 < N_L \in \mathbb{Z}^+$. This is relevant because similar ideas apply to the one-degree-of-freedom pitch rotational case.

In the following sections, we experimentally demonstrate that despite the fact that the microrobotic system is under-actuated, the pitch-angle can be controlled by biasing the average stroke angle away from zero, as depicted in Fig. 2-(b). The generation and measurement of pitch torques are described in the next subsection.

B. Static Experimental Setup and Pitch Torque Generation

The static experimental setup used in the *linear time-invariant* (LTI) system identification and control of the pitch torque dynamics is shown in Fig. 3. There, the most important element is the pitch torque sensor first presented in [7]. Its design and construction are reviewed briefly here. Conceptually, we desire to measure a single torque exerted by the flapping-wing microrobot (in this case, the pitch torque), while ignoring other forces and torques. Thus, we design an elastic beam that is compliant to torques about a single axis, and stiff to off-axis loading. The deformation of the beam under an applied load is then measured and converted to an analog voltage, which is calibrated to correspond to a torque value.

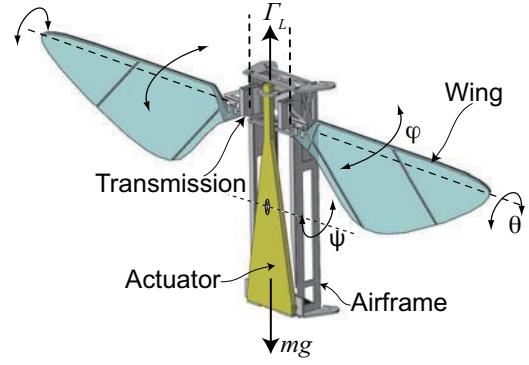


Fig. 1. Illustration of the microrobotic fly employed in the research presented in this article, similar to the one in [4]. This microrobot was entirely designed and fabricated by the authors at the Harvard Microrobotics Laboratory. Γ_L : Average lift force; φ : Flapping angle (also referred as stroke angle); θ : passive rotation angle; ψ : Pitch angle about the horizontal axis that intersects the robot's center of mass.

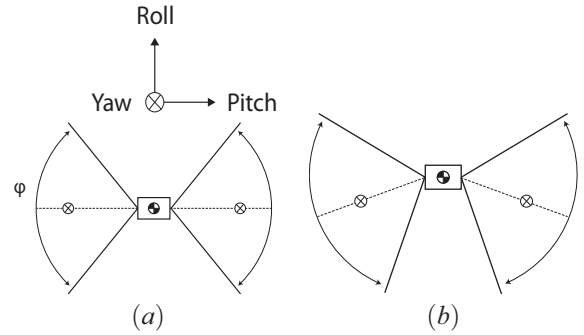


Fig. 2. (a): Symmetrical flapping. Ideally no body torques are generated and the angles of rotation in three dimensions about the robot's center of mass (pitch, roll and yaw) should stay at 0° . (b): Asymmetrical flapping, which allows the microrobotic system to produce torques about the pitch axis.

The sensor's elastic beam is illustrated in *magenta* in Fig. 4. This is a fixed-free cantilever beam with a '+'-shaped cross section, which is compliant to torques about its longitudinal axis, yet stiff to other torques and all three (x,y,z) forces. Torsion of the beam, and therefore rotation of the free end, causes displacement of two anti-symmetrical target plates. The displacement of the target plates is measured by capacitive probes (Microsense model 8810 gauging system and model 2813 probe head), which output ± 10 V analog signals. The beam itself is laser-cut from a 6-mil Invar sheet, selected for its low coefficient of thermal expansion (to minimize thermal drift), laser-welded and assembled. A CAD model of the complete sensing apparatus, including the supporting structures for mounting and holding the capacitive probes, is also shown in Fig. 4.

Optimization results of the beam geometry to maximize performance for the desired tests is presented in [7]. The sensor was calibrated by hanging weights at different radial positions and measuring the resulting voltage change. The final design has a range of $\pm 130 \mu\text{Nm}$, a resolution of 4.5 nNm , sensitivity of $75.8 \text{ mV}/\mu\text{Nm}$, and bandwidth of 800 Hz . These specifications prove more than sufficient for accurately characterizing the pitch torque response of a

robotic fly flapping its wings at 100 Hz. The microrobot is mounted to the sensor beam via a lightweight, laser-machined carbon fiber truss, as shown in Fig. 3. Both lift and drag forces are exerted on the fly's wings as they flap, as shown in Fig. 5, generating torques about the sensor beam's axis. For a nominally symmetric upstroke and downstroke, as in Fig. 2-(a), the time-averaged torque generated by drag forces should be zero. However, if the fly shifts its mean flapping angle forward or backward (for example, flapping from -40° to $+60^\circ$ instead of -50° to $+50^\circ$, the former case having an average flapping angle of $+10^\circ$ instead of 0°), the time-averaged torque generated by the flight forces will be nonzero. Thus the DC offset of the piezoelectric actuator can be used as a control input to modulate the time-averaged pitch torque.

III. TORQUE CONTROL EXPERIMENTS

In [1] and [3] it is shown that the vertical degree of freedom (altitude) can be controlled by modulating the average lift force, $\Gamma_L(\sigma)$ in Fig. 1. Analogously, the pitch-angle degree of freedom can be controlled by modulating the average torque produced by asymmetrical flapping as described in the previous section (Fig. 2-(b)). Thus, in this section we show experimental results on average torque control, using the static experimental setup described in Section II. The methodology and results presented in this section are essential in the design of the controller implemented in the rotational experiments discussed in the next section.

Here, the excitation to the actuator has the form

$$u(t) = \alpha_u(t) \sin(2\pi f_u t) + \beta_u(t), \quad (2)$$

where $\alpha_u(t)$ is chosen *a priori*, typically a constant, and $\beta_u(t)$ is the control signal computed according to a control law. A systems-and-signals block diagram representation of the experiment is shown in Fig. 6. The actuator driving the flapping-wing microrobot is excited with the analog representation (using a D/A converter) of the signal $u(t)$. The instantaneous torque is measured using the sensor described in the previous section and digitized using an A/D converter to obtain the discrete-time signal $\tau(t)$. The measured torque, $\tau(t)$, is filtered through an LTI system in order to compute an estimate of the average torque, labeled as $A_\tau(t)$. This is done to obtain the cycle-averaged torque, given the periodic nature of the instantaneous measurement. In this case, a natural estimating filter is a moving average, defined as

$$F_A(z) = \frac{1}{N_\tau} \sum_{i=0}^{N_\tau-1} z^{-i}, \quad (3)$$

where $0 < N_\tau \in \mathbb{Z}^+$ and $A_\tau(t) = F_A(z)\tau(t)$. This is a simple low-pass FIR filter, and therefore, $A_\tau(t)$ can be estimated using other low-pass dynamics. In general, an appropriate choice of the averaging filter can significantly increase the speed response of the estimation dynamics. This notion will be discussed in detail later in this section. Through out this section, a *Mathworks* xPC-target system is used for digital signal processing and control, running at a sample-and-hold rate of 10 KHz.

The previous definitions allows one to think of the whole experimental system as an input-output mapping that can be identified using LTI system identification methods, provided

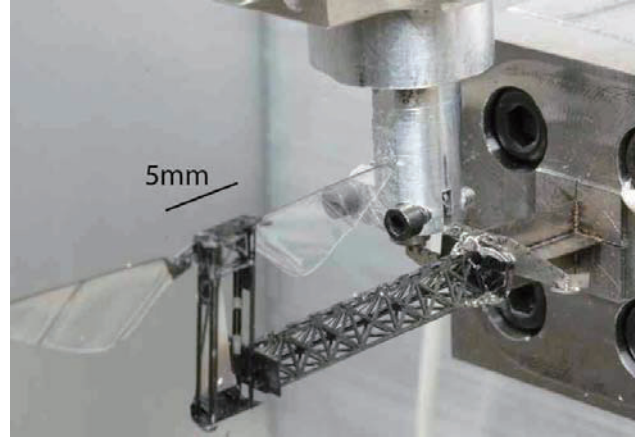


Fig. 3. Photograph of the experimental setup used in the static LTI system identification and control of the pitch torque dynamics.

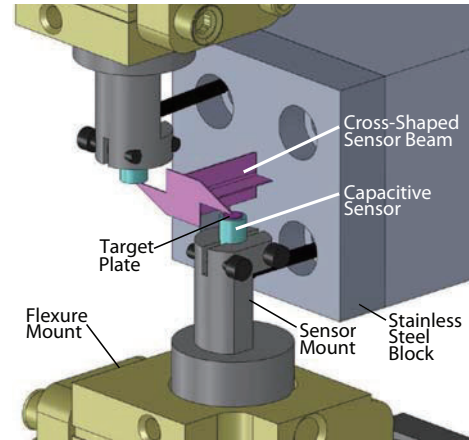


Fig. 4. 3-D CAD model of the torque sensor used in the static pitch control experiments. The cross-shaped elastic beam is shown in magenta. The capacitive probes are shown in cyan.

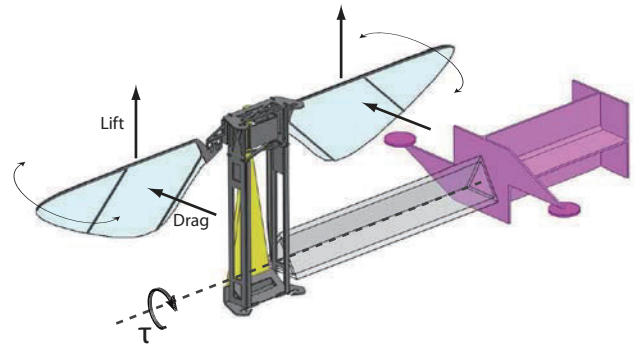


Fig. 5. Illustration of the flapping-wing microrobot mounted to the torque sensor, showing the location of lift and drag forces acting on the wings, and resulting instantaneous torque τ about the sensor beam axis. The average pitch torque is modulated by shifting the DC position of the wings during flapping.

that $\alpha_u(t)$ is constant and f_u is fixed. This notion is illustrated in Fig. 7. An LTI model $\hat{T}(z)$ of the idealized system dynamics $T(z)$, with the fixed frequency $f_u = 100$ Hz, is estimated using the subspace system identification algorithm

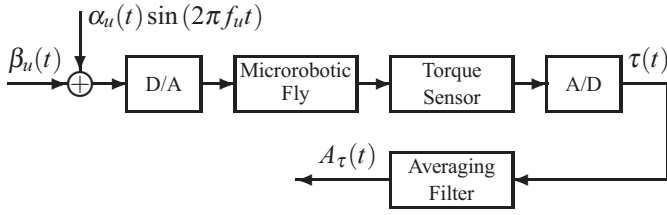


Fig. 6. Block diagram of the system used in the torque control experiments.

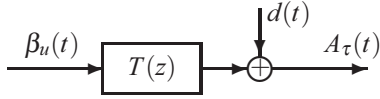


Fig. 7. Idealized system dynamics. $T(z)$: Discrete-time open-loop plant; $\beta_u(t)$: Bias control signal; $A_\tau(t)$: Estimate of the average torque, computed in real time using the instantaneous torque signal $\tau(t)$; $d(t)$: Output disturbance, representing the aggregated effects of all the disturbances affecting the system, including stochastic wind currents.

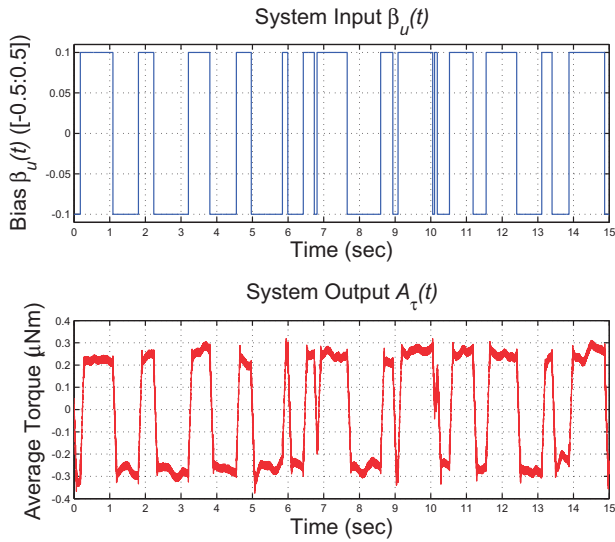


Fig. 8. Excitation signal (upper plot) and corresponding output (bottom plot) used in the system identification of $T(z)$, for $f_u = 100$ Hz and $a_u(t) = 0.5$ (constant).

$n4sid$ [8], after exciting the system with a *pseudo random binary signal* (PRBS) [9]. A section of the employed exciting PRBS and the corresponding output are shown in Fig. 8. The resulting $\hat{T}(z)$ is shown on the left in Fig. 9. Here, the magnitude of $\hat{T}(z)$ displays two relevant features. The first is the low-pass shape over the low-frequency range, which corresponds to the true dynamics of the mapping from $\beta_u(t)$ to $A_\tau(t)$ (i.e., no sensor noise is affecting the measurement of $\tau(t)$). The second is the peak at 800 Hz approximately, which corresponds to the sensor resonant frequency. We will show later that the exciting signal $u(t)$, when the system is under an appropriate control law, does not significantly excite the sensor resonance.

Using the model $\hat{T}(z)$, an LTI control law with the form

$$\beta_u(t) = K_\tau(z)e_\tau(t) = K_\tau(z) \left[A_\tau^{(r)}(t) - A_\tau(t) \right] \quad (4)$$

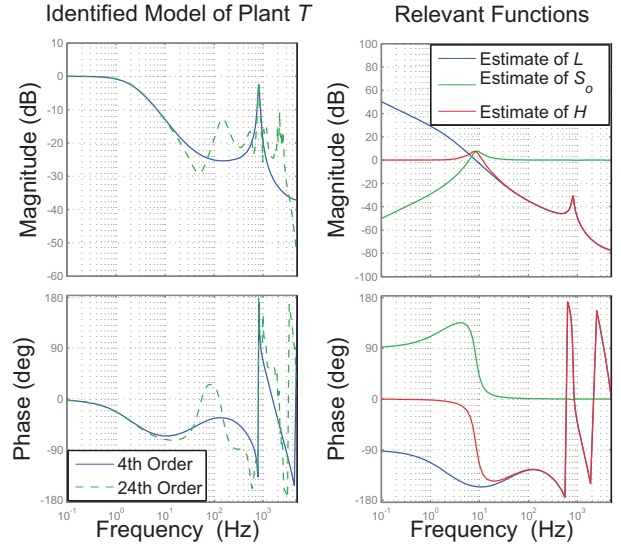


Fig. 9. *Left Plot*: Bode diagram of the identified model $\hat{T}(z)$ of the plant $T(z)$. A 24th-order model was originally identified (in green), a reduced 4th-order model is shown in blue. *Right Plot*: Estimate \hat{L} of the loop-gain function $L = TK_\tau$, shown in blue. Estimate $\hat{S}_o = (1 + \hat{T}K_\tau)^{-1}$ of the output sensitivity function $S_o = (1 + TK_\tau)^{-1}$, shown in green. Estimate $\hat{H} = \hat{T}K_\tau(1 + \hat{T}K_\tau)^{-1}$ of the complementary sensitivity function $H = TK_\tau(1 + TK_\tau)^{-1}$, shown in red.

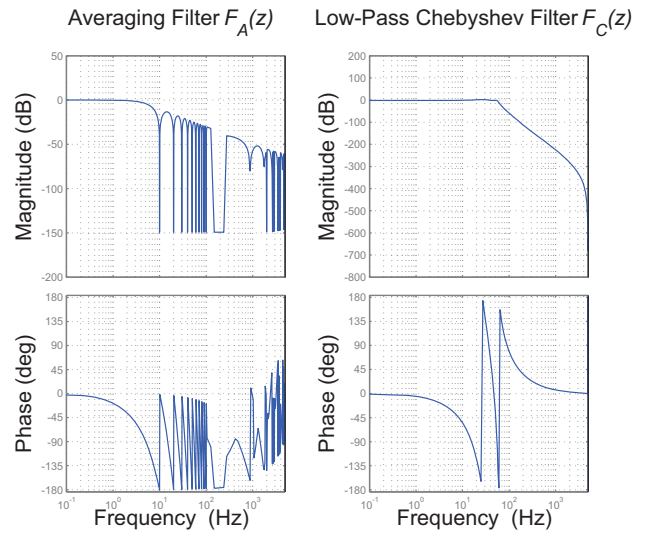


Fig. 10. *Left Plot*: Averaging filter $F_A(z) = \frac{1}{N_\tau} \sum_{i=0}^{N_\tau-1} z^{-i}$. *Right Plot*: Low-pass Chebyshev filter $F_C(z)$.

is found, where $A_\tau^{(r)}(t)$ is a reference and $A_\tau(t)$ is the average torque in Fig. 6. The controller $K_\tau(z)$ is generated using classical techniques of loop shaping. The stability, performance and stability robustness of the resulting closed-loop system is analyzed using classical techniques. To this end, estimates of the loop-gain function $L = TK_\tau$, the output sensitivity function $S_o = (1 + TK_\tau)^{-1}$, and the complementary sensitivity function $H = TK_\tau(1 + TK_\tau)^{-1}$, employing the estimate \hat{T} , are found. The resulting Bode plots of the estimates, labeled \hat{L} , \hat{S}_o and \hat{H} respectively, are shown on the right in Fig. 9.

The main objectives of a control strategy are to increase

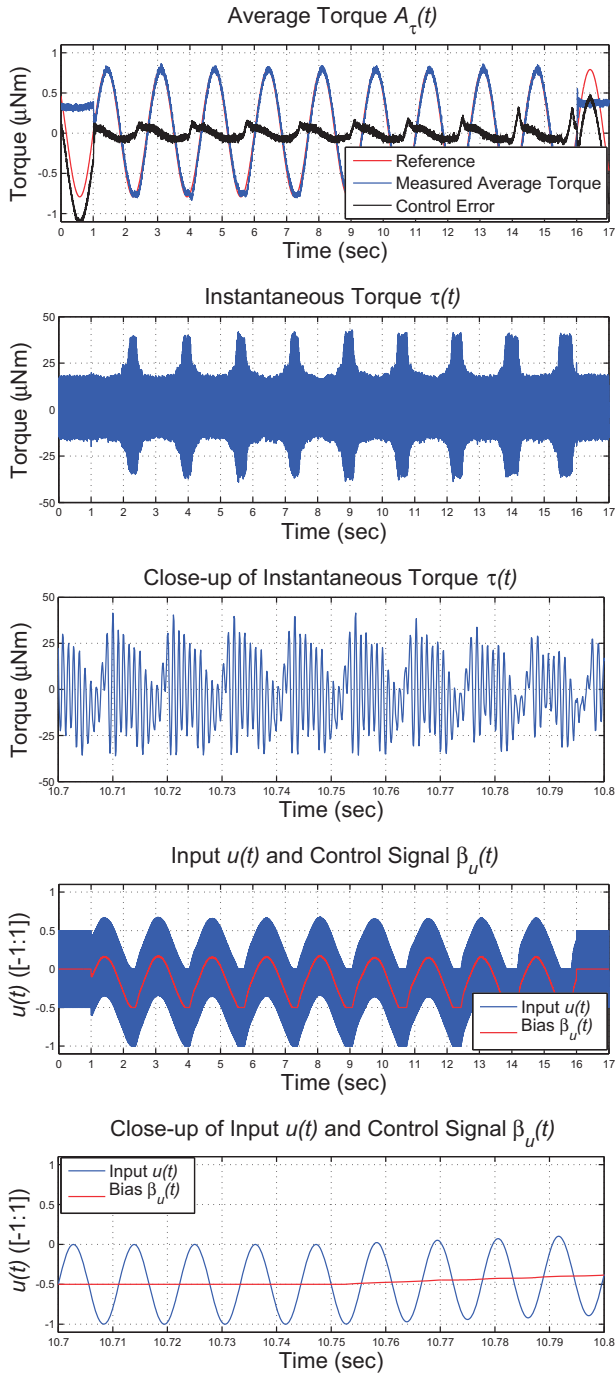


Fig. 11. **Experimental Case 1.** *First Row:* Average torque reference $A_\tau^{(r)}(t)$ (red), average torque measurement $A_\tau(t)$ (blue) and control error $e_\tau(t)$ (black). *Second Row:* Instantaneous torque $\tau(t)$. *Third Row:* Close-up of instantaneous torque $\tau(t)$. *Fourth Row:* Input $u(t)$ (blue) and control signal $\beta_u(t)$ (red). *Fifth Row:* Close-up of input $u(t)$ (blue) and control signal $\beta_u(t)$ (red).

the system bandwidth and simultaneously reject disturbances (usually low-frequency), while maintaining the stability of the closed-loop configuration. From the Bode plots of \hat{L} , \hat{S}_o and \hat{H} , it is clear that these objectives are achieved. The fulfillment of the first objective follows from noticing that H maps the desired average torque $A_\tau^{(r)}(t)$ to the measured average torque $A_\tau(t)$, and that the bandwidth of \hat{H} is sig-

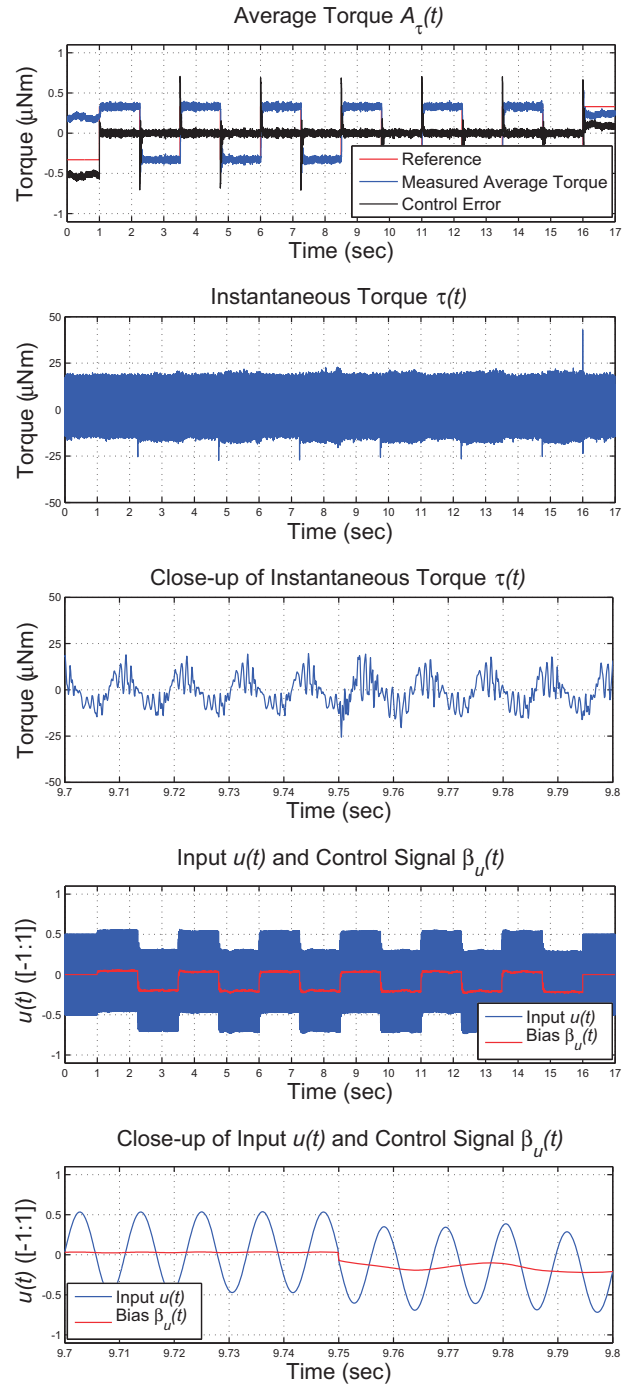


Fig. 12. **Experimental Case 2.** *First Row:* Average torque reference $A_\tau^{(r)}(t)$ (red), average torque measurement $A_\tau(t)$ (blue) and control error $e_\tau(t)$ (black). *Second Row:* Instantaneous torque $\tau(t)$. *Third Row:* Close-up of instantaneous torque $\tau(t)$. *Fourth Row:* Input $u(t)$ (blue) and control signal $\beta_u(t)$ (red). *Fifth Row:* Close-up of input $u(t)$ (blue) and control signal $\beta_u(t)$ (red).

nificantly wider than the bandwidth of \hat{T} . The fulfillment of the second objective follows from noticing that in closed loop, S_o maps the output disturbance $d(t)$ to the measured average torque $A_\tau(t)$, and that \hat{S}_o is a high-pass filter. The shapes of the resulting \hat{H} and \hat{S}_o are completely explained by the so-called “waterbed effect”, a direct consequence of

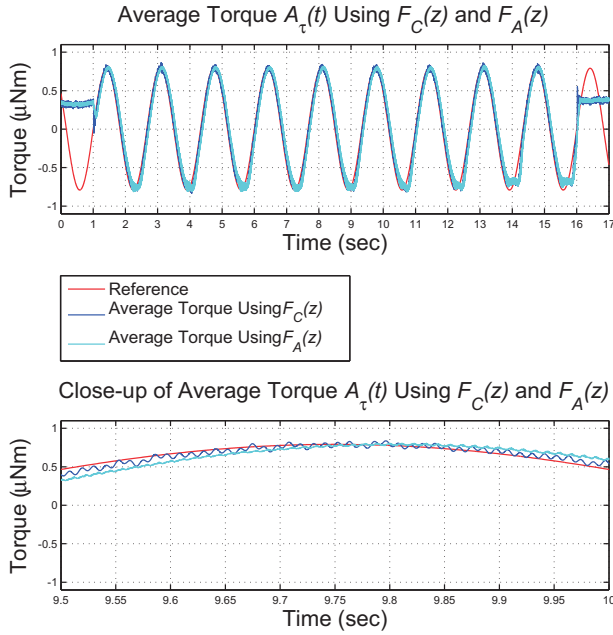


Fig. 13. Comparison of the average torque signals $A_\tau(t)$ estimated using the filters $F_C(z)$ (in blue) and $F_A(z)$ (in light blue), corresponding to the **experimental case 1**. Here, the measurement used in the controller implementation is the output from $F_C(z)$. Note that the intuitive most obvious estimate of the average torque is the output from $F_A(z)$. *Upper Plot*: The complete sequence. *Bottom Plot*: Close-up of the upper plot.

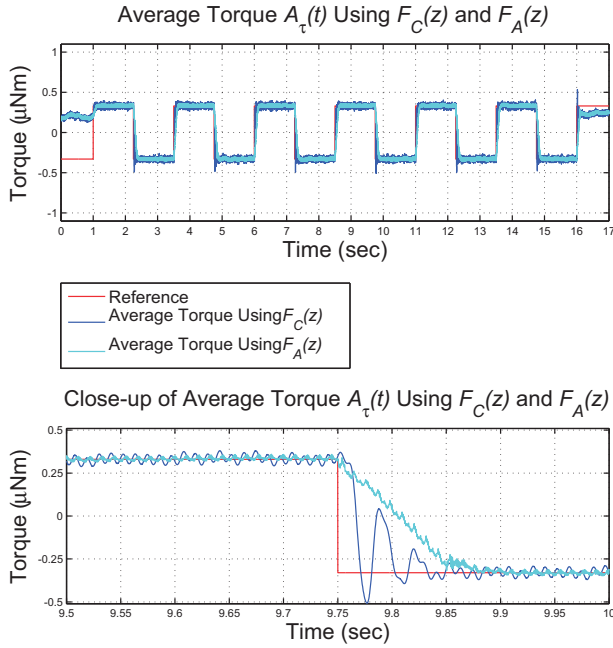


Fig. 14. Comparison of the average torque signals $A_\tau(t)$ estimated using the filters $F_C(z)$ (in blue) and $F_A(z)$ (in light blue), corresponding to the **experimental case 2**. Here, the measurement used in the controller implementation is the output from $F_C(z)$. Note that the intuitive most obvious estimate of the average torque is the output from $F_A(z)$. *Upper Plot*: The complete sequence. *Bottom Plot*: Close-up of the upper plot.

the *Bode sensitivity integral theorem* [10]. From the Bode plot of \hat{L} , the stability and stability robustness of the system can be evaluated using the classical indices minimum phase and gain margins. In this case those are 24.5 deg and 45 dB,

respectively.

Before discussing experimental results, we discuss the possibility of using a different choice of filter, and not $F_A(z)$ directly, to estimate the average torque. The main reason for attempting this is that any time-delay reduction in the resulting closed-loop system increases the speed and robustness of the system as a whole. Here, we employ a Chebyshev type 1 low-pass filter, which is shown on the right in Fig. 10, labeled as $F_C(z)$. Next to $F_C(z)$ is the frequency response of $F_A(z)$. As can be seen there, $F_C(z)$ was designed so that its bandwidth is similar to the bandwidth of $F_A(z)$. The main difference between both filters is that the order of $F_A(z)$ is significantly larger than the order of $F_C(z)$, 1,000 and 8 respectively. Note that the order of a given filter is directly related to its speed of response. As demonstrated with the following experimental results, the switch from $F_A(z)$ to $F_C(z)$ provides the control system as a whole with several desirable features.

The control system capabilities are demonstrated through two experimental cases. In the first case, shown in Fig. 11, the control system is asked to track a sinusoidal average pitch torque reference. In Fig. 11, the first row shows the average torque reference $A_\tau^{(r)}(t)$, the resulting average torque measurement $A_\tau(t)$ and the control error $e_\tau(t)$, using the Chebyshev type 1 filter on the right in Fig. 10. The second row shows the measured instantaneous pitch torque $\tau(t)$ required for following the reference $A_\tau^{(r)}(t)$. A close-up of this signal is shown in the third row. The fourth row shows the control signal $\beta_u(t)$ and the input to the actuator $u(t)$. A close-up showing short sections of $u(t)$ and $\beta_u(t)$ are shown in the fifth row.

The second case is shown in Fig. 12, where the control system is asked to track a square-wave reference. Here, the most interesting thing to notice is the signals $\beta_u(t)$ and $u(t)$ in the fourth row. The control signal $\beta_u(t)$ changes abruptly in order to make the system to follow the square-wave reference. Interestingly, the input to the actuator $u(t)$ varies smoothly, which prevents the piezoelectric actuator from being damaged. Figs. 13 and 14 compare the signals $A_\tau(t)$, obtained using $F_C(z)$ and $F_A(z)$, for the two cases explained in the previous paragraphs. Two important things should be noted in these plots. The first is that using the output from $F_C(z)$ as the measurement for control, the estimated average torque computed using $F_A(z)$ closely follows the reference. The second is that the resulting signal $A_\tau(t)$ computed using $F_A(z)$ is both slower and smoother than $A_\tau(t)$ computed using $F_C(z)$, as expected.

IV. PITCH-ANGLE CONTROL EXPERIMENTS

In the previous section, using the static experimental setup in Fig. 3, we gathered key information about the microrobot, and using this information, a strategy for controlling average pitch torque was devised. The results clearly show that in principle the pitch angle ψ can be controlled, provided that high quality sensors are used in this task. In this section, we use the experimental setup in Fig. 15 for pitch-angle control experiments. Here, a robotic fly is suspended by a thin wire that passes approximately through the center of mass, as shown on the right in Fig. 16. This mechanical configuration allows the robot to freely rotate around the

wire, which is the pitch-angle to be controlled. Two safety wires are added to the experimental apparatus in order to prevent the robotic fly from spinning, in case the system becomes unstable. The pitch-angle ψ is estimated using a *Vicon motion capture system* (MCS). The MCS uses six cameras that detect the position, relative to a preset inertial frame, of reflective markers glued to the robot's airframe. Using the information from the markers' position, through the 3-D object tracking software *Tracker*, the pitch-angle ψ is estimated. A picture of three of the reflective markers on the airframe is shown on the left in Fig. 16.

In this case, the dynamical equation relating instantaneous torque and pitch-angle is simply

$$J_o \ddot{\psi}(\sigma) = \tau_o(\sigma), \quad (5)$$

where J_o is the moment of inertia with respect to the center of mass and τ_o is the torque around the center of mass. Note that there exists a one-to-one mapping from the torque $\tau(\sigma)$, measured as described in Section III, to $\tau_o(\sigma)$. Also note that the operator input-output representation of (5) is

$$\psi(\sigma) = \left[\frac{1}{J_o s^2} \tau_o \right] (\sigma). \quad (6)$$

This is a low-pass unstable double-integrator filter, which implies that the oscillatory instantaneous torque τ_o is low-pass filtered by the dynamics of the system. Therefore, $\psi(\sigma)$ can be interpreted as an estimate of the average torque produced by the asymmetrical flapping of the wings, as shown in Fig. 2-(b). Thus, it is reasonable to implement a control law with the form

$$\beta_u(t) = \lambda K_\tau(z) e_\psi(t) = \lambda K_\tau(z) [\psi_d(t) - \hat{\psi}(t)], \quad (7)$$

where $\psi_d(t)$ is a pitch-angle reference signal, $\hat{\psi}(t)$ is the estimate of ψ , obtained using the *Vicon* system, and $\lambda \in \mathbb{R}$ is a tuning parameter.

In contrast to the torque control case in Section III, in this case the sensor noise cannot be considered negligible for two reasons. The first is that due to the high computational burden required by the MCS to estimate the angle ψ , data from the *Vicon* system to the digital signal processor is sent at a rate of 500 Hz. As explained in Section III, the controller runs at 10 KHz, which implies that from the controller viewpoint, the measurement of ψ is updated every 20 sampling steps. The second source of measurement noise is numerical errors produced by the estimation process and discontinuities in the tracking process. This phenomenon might be due to the very small size of the microrobot and the reflective markers relative to the tracking cameras, as shown in Fig. 15. Thus, it is possible to think of the measurement as $\hat{\psi}(t) = \psi(t) + n_\psi(t)$, where n_ψ is sensor noise that might significantly decrease the performance and stability robustness of the system resulting from using the scaled controller $\lambda K_\tau(z)$, designed in Section III. Adjusting the tuning parameter λ , satisfactory results are experimentally obtained. This is the first demonstration of pitch angle control for an insect-sized robot. A typical example is shown in Figs. 17 and 18. Here, the system is asked to follow a 0.1 Hz sinusoidal reference (in red in Fig. 17). The resulting measurement is shown in blue. A high-speed video sequence of five frames of the experiment is shown in Fig. 18 (upper

pictures). The corresponding model captured and built by the MCS at the same sampled instants is shown on the bottom in Fig. 18. A supporting movie of the whole experiment can be found at [11].

V. CONCLUSION AND FUTURE WORK

We presented a method for designing and implementing strategies for torque and pitch-angle control of a flapping-wing microrobot. Here, we followed the design philosophy introduced in [1], [2] and pursued in [3], in the context of lift-force and altitude control of flapping-wing flying microrobots. First, we designed and built a static experimental apparatus that allows us to measure instantaneous torques produced by asymmetrical flapping patterns enforced on the microrobot, while rigidly connected to a torque sensing device. Then, we use modern LTI system identification techniques for gathering essential information about the microrobotic system, which is used for designing, implementing and evaluating feedback controllers in a hardware-in-the-loop fashion, employing a static experimental apparatus. We provided compelling empirical evidence that the original pitch-angle control problem can be transformed into one of torque control, and therefore, the same strategy can be implemented for average torque control and pitch-angle control.

One of the main practical contributions in this article is the empirical demonstration that motion capture systems can be employed as sensors for measuring the degrees of freedom of moving robots on the scale of insects. It is important to emphasize that this is the first demonstration of pitch control for an at-scale flapping-wing robotic insect. This is an essential capability in order to achieve the goal of untethered flight of flapping-wing microrobots, as the one considered here.

REFERENCES

- [1] N. O. Pérez-Arancibia, J. P. Whitney, and R. J. Wood, "Lift Force Control of a Flapping-Wing Microrobot," in *Proc. 2011 Amer. Cont. Conf.*, San Francisco, CA, Jul. 2011, pp. 4761–4768.
- [2] N. O. Pérez-Arancibia, J. P. Whitney, and R. J. Wood, "Lift Force Control of Flapping-Wing Microrobots Using Adaptive Feedforward Schemes," to appear in *IEEE/ASME Trans. Mechatron.*, 2011.
- [3] N. O. Pérez-Arancibia and K. Y. Ma and K. C. Galloway and J. D. Greenberg and R. J. Wood, "First Controlled Vertical Flight of a Biologically Inspired Microrobot," *Bioinspir. Biomim.*, vol. 6, no. 3, pp. 036 009–1–11, Sep. 2011.
- [4] R. J. Wood, "The First Takeoff of a Biologically Inspired At-Scale Robotic Insect," *IEEE Trans. Robot.*, vol. 24, no. 2, pp. 341–347, Apr. 2008.
- [5] B. M. Finio and R. J. Wood, "Distributed power and control actuation in the thoracic mechanics of a robotic insect," *Bioinspir. Biomim.*, vol. 5, no. 4, pp. 045 006–1–12, Dec. 2010.
- [6] J. P. Whitney and R. J. Wood, "Aeromechanics of passive rotation in flapping flight," *J. Fluid Mech.*, vol. 660, pp. 197–220, Oct. 2010.
- [7] B. M. Finio, K. C. Galloway, and R. J. Wood, "An ultra-high precision, high bandwidth torque sensor for microrobotics applications," in *Proc. IEEE/RSS Int. Conf. Intell. Robots Syst.*, San Francisco, CA, Sep. 2011, pp. 31–38.
- [8] P. Van Overschee and B. De Moor, *Subspace Identification for Linear Systems*. Boston, MA: Kluwer, 1996.
- [9] L. Ljung, *System Identification*. Upper Saddle River, NJ: Prentice Hall, 1999.
- [10] S. Skogestad and I. Postlethwaite, *Multivariable Feedback Control*. Chichester, England: Wiley, 1996.
- [11] N. O. Pérez-Arancibia, P. Chirarrattananon, B. M. Finio, and R. J. Wood, "S1," URL: <http://micro.seas.harvard.edu/RoBio2011/S1.mp4>, Aug. 2011.

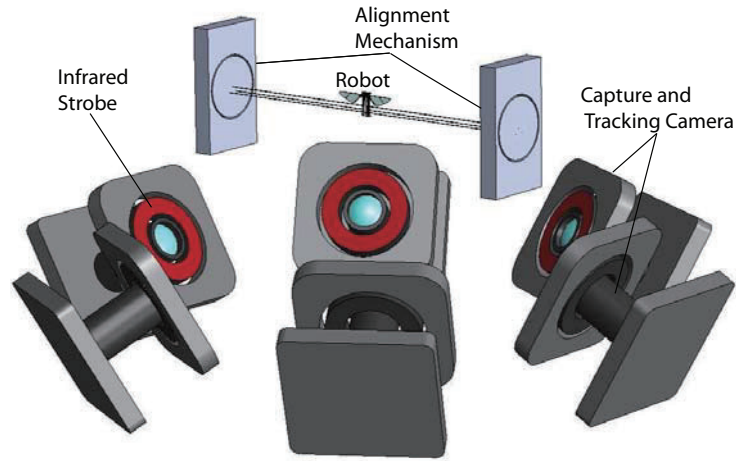
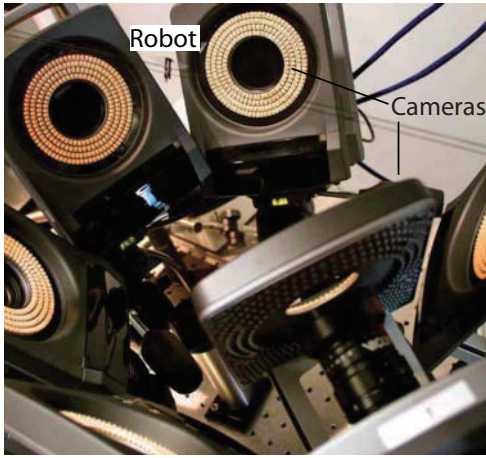


Fig. 15. Experimental setup used in the pitch-angle control experiments. *Left Plot*: Photograph showing the microrobotic fly, which is suspended by a thin wire that passes through its airframe. The motion capture-and-tracking system uses six high-speed cameras that detect and track reflective markers glued to the microrobot. *Right Plot*: Illustration of the experimental apparatus (not to scale).

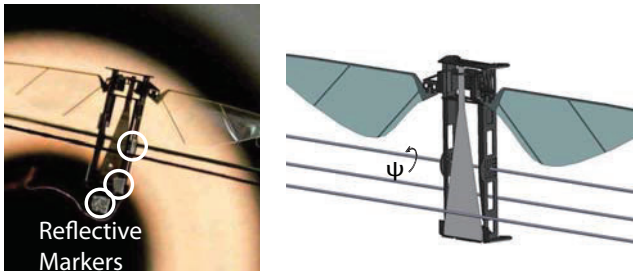


Fig. 16. *Left Plot*: Close-up of the microrobot showing the reflective markers used by the *Vicon* system to estimate the pitch-angle ψ . *Right Plot*: Illustration depicting the controlled variable, the pitch-angle ψ .

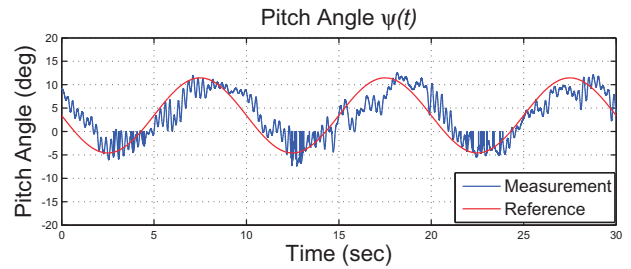


Fig. 17. Experimental example of pitch-angle control. Measurement/estimate $\hat{\psi}(t)$ in blue and reference $\psi_d(t)$ in red.

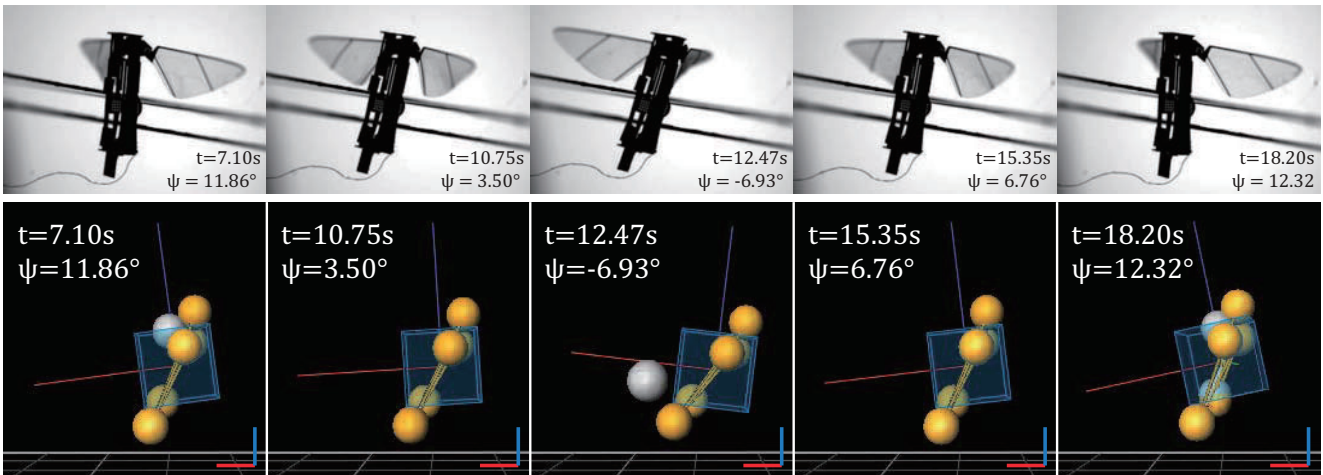


Fig. 18. *Upper Sequence*: Video sequence showing five frames of the experiment in Fig. 17. *Bottom Sequence*: Corresponding model captured and built by the motion capture system (*Vicon-Tracker*). The yellow spheres indicate the position of the true reflective markers. The white spheres indicate the position of wrongly detected non-existing markers. Detection of false markers are seen as sensor noise by the controller $K_{\tau}(z)$.